Journal of Applied Fluid Mechanics, Vol. 14, No. 2, pp. 345-359, 2021.
Available online at www.jafmonline.net, ISSN 1735-3572, EISSN 1735-3645.
DOI: 10.47176/jafm.14.02.31584

A Block–Interface Approach for High–Order Finite–Difference Simulations of Compressible Flows

M. Allahyari[1], K. Yousefi[2], V. Esfahanian[†3] and M. Darzi[4]

[1] *Department of Mechanical & Aerospace Engineering, University of Florida, Gainesville, FL 32611 USA*
[2] *Department of Mechanical Engineering, University of Delaware, Newark, DE 19716 USA*
[3] *Department of Mechanical Engineering, University of Tehran, Tehran, Iran*
[4] *Department of Mechanical & Aerospace Engineering, University of Missouri, Columbia, MO 65211 USA*

† *Corresponding Author Email*: *evahid@ut.ac.ir*

(Received March 13, 2020; accepted July 10, 2020)

ABSTRACT

The application of the high-order accurate schemes with multi-block domains is essential in problems with complex geometries. Primarily, accurate block-interface treatment is found to be of significant importance for precisely capturing discontinuities in such complex configurations. In the current study, a conservative and accurate multi-block strategy is proposed and implemented for a high-order compact finite-difference solver. For numerical discretization, the Beam-Warming linearization scheme is used and further extended for three-dimensional problems. Moreover, the fourth-order compact finite-difference scheme is employed for spatial discretization. The capability of the high-order multi-block approach is then evaluated for the onedimensional flow inside a Shubin nozzle, two-dimensional flow over a circular bump, and three-dimensional flow around a NACA 0012 airfoil. The results showed a reasonable agreement with the available exact solutions and simulation results in the literature. Further, the proposed block-interface treatment performed quite well in capturing shock waves, even in situations that the location of the shock coincides with block interfaces.

Keywords: Multi-block; Compact scheme; Block-interface; Shock.

1. INTRODUCTION

Although several high-order schemes have been developed over the past few decades to deal with a diverse range of problems (e.g., Shu and Osher,1988; Spotz and Carey, 1995; Colin and Rudgyard,2000; Qiu and Shu, 2011; Yang *et al.* 2015; Shu, 2016; Rahbari and Scalo, 2017; Xiong *et al.* 2018; Allahyari and Mohseni, 2017, 2018), applying high-order and high-accuracy methods to complex geometries is still limited. This is partly due to difficulties in keeping the accuracy of high order methods inside the domain and physical boundaries and also high computational costs of such methods. The finite volume methods, finite element methods, and discontinuous Galerkin schemes are popular in solving complex geometry problems with unstructured grids mainly due to their flexibility on arbitrary grids. The Finite-Difference Methods (FDMs) with structured meshes, however,are one of the proper methods in treating boundary layer flows (e.g., Blottner, 1975; Deng *et al.* 2012) because of their cost-effectiveness and simplicity. In order to apply high-order finite difference schemes to problems with complex geometries, it is required to decompose the computational domain into geometrically simpler blocks in which grid generation can be significantly facilitated. High-order multiblock FDMs are quite common in the numerical solution of fluid flows over non-trivial geometries. The main difficulties in multi-block interface strategies are, however, boundary conditions and instability at the block interfaces between sub-domains.

Compact FDMs offer additional advantages compared to their non-compact counterparts (see Dennis and Hudson, 1989; Li *et al.* 1995; Cui, 2009; Esfahanian *et al.* 2013, Allahyari *et al*., 2020). High-order compact finite difference schemes (Hirsh, 1975; Lele, 1992) are thus widely employed in various fields of computational fluid dynamics. Compact schemes are particularly popular in Direct Numerical Simulation (DNS) and Large Eddy Simulation (LES) of turbulent flows (e.g., Erlebacher *et al.* 1992; Visbal and Rizzetta, 2002; Kawai and Lele, 2010) and computational aeroacoustics (e.g., Freund *et al.* 2000; Freund, 2001; Colonius and Lele, 2004; Schaupp *et al.* 2008,

Rahbari and Paniagua, 2020) because of their spectral-like resolution, short size stencil, low dispersion and diffusion errors, and high-order accuracy.

The early studies of multi-block strategies include those of Atta (1981), Hessenius and Pulliam (1982), Rai and Chakravarthy (1984), Rai (1986, and Hessenius and Rai (1986), among others. The application of different overlapping zonal grids for solving full-potential equations was investigated by Atta (1981) to obtain the transonic flow field about complex configurations (see also Atta and Vadyak, 1982; Benek *et al.* 1983). The computed results around a two-dimensional (2D) airfoil configuration showed an accurate and stable scheme, and overall, led to reduced computational costs. Hessenius and Pulliam (1982) presented a conservative block interface condition for solving one- and two-dimensional Euler equations with implicit schemes. It was most importantly shown that the conservative treatment of boundary conditions at block interfaces is required for problems with discontinuities, e.g., shock waves. Rai and Chakravarthy (1984) employed the Osher upwind scheme in conjunction with multiblock grids, which have metric discontinuities at block interfaces, to solve the Euler equations for inviscid flow problems. The results demonstrated the abilities of the multi-block approach in capturing shock waves in flow fields with complicated shock patterns, including nozzle flow, supersonic flowover a cylinder, and shock-wave diffraction by a ramp. Furthermore, Rai (1986) developed a conservative zonal-boundary scheme for the solution of Euler equations in which discontinuities were observed to smoothly move from one sub-domain to another through block boundaries. In a similar study, Hessenius and Rai (1986) also explored the interface treatments, based on the zonal-boundary scheme proposed by Rai (1986), for using with patched, discontinuous grid system around supersonic blunt bodies. The high-order interface treatment methodologies are broadly applied for the purpose of parallel processing (see Lien *et al.*, 1996; Esfahanian *et al.*, 2013; Morgan *et al.*, 2001, 2006). For instance, Rousta and Lessani (2020) studied near-wall heat transfer in particle-laden turbulent flows using a high-order solver where the computational domain can be decomposed into rectangular blocks in the message passing interface (MPI) approach.

The interface schemes developed in a series of studies by Hessenius and Pulliam (1982), Rai and Chakravarthy (1984), Rai (1986), and Hessenius and Rai (1986) were based on the zonal or patched-grid approach that could be employed with first- and second-order-accurate integration schemes for Euler equations. The interface conditions were accordingly adopted for the highorder accurate numerical solution of compressible and incompressible Navier-Stokes equations. The overset-grid (or equivalently finite-sized overlap) approach (Atta, 1981; Benek *et al.* 1983) is a relatively straightforward and yet powerful tool providing a high-order interface treatment for numerical simulation of complex fluid flows. The oversetgrid methods, in which the computational region is divided into overlapping blocks, have been investigated in many studies (e.g., Lien *et al.* 1996; Visbal and Gaitonde, 1999; Gaitonde and Visbal, 2000; Sherer and Scott, 2005; Sherer and Visbal, 2007; Wang *et al.* 2014; Koblitz *et al.* 2017). In order to study turbulence, Lien *et al.* (1996) examined the application of a multi-block algorithm for different turbulent flow cases, including the turbulent flow over an airfoil with trailing-edge flap. In their multi-block implementation, the communication between adjacent blocks was handled by a twocell overlap region through connectivity matrices, and consequently, an improved numerical resolution and parallel computingwere reported. Gaitonde and Visbal (2000) further investigated the effects of the finite-sized overlap method on stability and accuracy of interface treatments when high-order compact finite-difference schemes were used to solve Navier-Stokes equations in general curvilinear coordinates (see also Gaitonde and Visbal, 1999). It was observed that a five-point overlap in the region between neighboring blocks is sufficient to preserve the interior high-order (i.e. minimum fourth-order) differencing schemes. The same overset-grid approach was later employed by Morgan *et al.* (2001) and Morgan *et al.* (2006) to develop a high-order compact finite-difference Navier–Stokes solver for LES and DNS simulations and by Rizzetta *et al.* (2008) to investigate the active flow control over different complex geometries. In numerical simulations of fluid flows using a multi-block high-order accurate scheme, employing a proper block interface treatment is essential, particularly in precisely capturing flow discontinuities. In this paper, a block-interface approach is introduced and adopted into a high-order compact finite difference solver for predicting fluid flow problems. The proposed method is conservative in the presence of shock and other discontinuities and preserves the accuracy of compact finite-difference solutions. It is also easily implemented, and that avoids additional complexities in the numerical algorithm.

Here, the multi-block high-order solver is implemented for various flow conditions and geometries, including one-dimensional (1D) fluid flow inside a Shubin nozzle, 2D channel flow with a bump, and three-dimensional (3D) flow around a NACA 0012 airfoil, with the fourth-order compact scheme for spatial discretizations. The multi-block strategy proposed in the current work can also be directly extended for simulations of turbulent flows with turbulence transition and complex geometries, and further, for high-performance computing applications.

The rest of this paper is organized as follows. The dynamical governing equations are derived in section 2. Numerical discretization methods and time advancement procedures are described in section 3. In section 4, the multi-block strategy and its performance in comparison with a singleblock solution are explained. The results are presented in section 5, confirming the suitability of the multi-block high-order solver in dealing with shocks and its performance over a single-block strategy. Finally, section 6 provides a brief conclusion.

2. GOVERNING EQUATIONS

In this section, we are introducing the nondimensional governing equations of compressible fluid flow, including conservation of mass, momentum, and energy in a general curvilinear coordinate system. For a general curvilinear coordinate system with (ξ,η,ζ) coordinates, the transformed Navier-Stokes equations can be written in the conservation form for time-dependent domains as

$$\frac{\partial \mathbf{U}}{\partial \mathrm{t}}+\frac{\partial}{\partial \xi}\left(\mathbf{F}-\frac{1}{Re}\mathbf{F}_{\mathrm{v}}\right)+\frac{\partial}{\partial \eta}\left(\mathbf{G}-\frac{1}{Re}\mathbf{G}_{\mathrm{v}}\right)+\frac{\partial}{\partial \xi}\left(\mathbf{H}-\frac{1}{Re}\mathbf{H}_{\mathrm{v}}\right)=0 \tag{1}$$

Here t is the time, $\mathbf{U}$ is the conserved variable vector**,** $\mathbf{F}$, $\mathbf{G}$, and $\mathbf{H}$ are the convective flux vectors, $\mathbf{F}_{\upsilon}$, $\mathbf{G}_{\upsilon}$, and $\mathbf{H}_{\upsilon}$ are the viscous flux terms, and Re is the reference Reynolds number. The vector of conserved variables is given by

$$\boldsymbol{U}=J^{-1}\begin{bmatrix}\rho\\ \rho u\\ \rho v\\ \rho w\\ E\end{bmatrix} \tag{2}$$

and the vectors of convective fluxes are defined as

$$\mathbf{F}=J^{-1}\begin{bmatrix}\rho U\\ \rho uU+\xi_x p\\ \rho vU+\xi_y p\\ \rho wU+\xi_z p\\ (E+p)U\end{bmatrix},, \tag{3a}$$

$$\mathbf{G}=J^{-1}\begin{bmatrix}\rho V\\ \rho uV+\eta_x p\\ \rho vV+\eta_y p\\ \rho wV+\eta_z p\\ (E+p)V\end{bmatrix},, \tag{3b}$$

$$\mathbf{H}=J^{-1}\begin{bmatrix}\rho W\\ \rho uW+\zeta_x p\\ \rho vW+\zeta_y p\\ \rho wW+\zeta_z p\\ (E+p)W\end{bmatrix}. \tag{3c}$$

In these equations,

$$\begin{aligned}U&=\xi_x u+\xi_y v+\xi_z w,\\ V&=\eta_x u+\eta_y v+\eta_z w,\\ W&=\zeta_x u+\zeta_y v+\zeta_z w,\end{aligned} \tag{4}$$

are contravariant velocities in directions normal to the constant ξ, η, and ζ surfaces, respectively, and

$$J=\frac{\partial(\xi,\eta,\zeta)}{\partial(x,y,z)}=\Big[x_\xi\left(z_\zeta y_\eta-z_\eta y_\zeta\right)-x_\eta\left(y_\xi z_\zeta-z_\xi y_\zeta\right)+x_\zeta\left(y_\xi z_\eta-z_\xi y_\eta\right)\Big]^{-1} \tag{5}$$

is the Jacobian of the transformation. Moreover, (u,v,w) are the Cartesian velocity components in (x,y,z) directions, ρ is the density, p is the pressure, and E is the total energy. We note here that all variables appeared in these equations are accordingly non-dimensionalized by appropriate reference values, i.e. the cartesian and curvilinear coordinates by the characteristic length L, velocity components by the reference velocity u_∞, density and viscosity by the free-stream density and viscosity, pressure by $\rho_\infty u_\infty{}^2$, and time by L/u_∞, leading to the definition of the reference Reynolds number $Re=\rho_\infty u_\infty L/\mu_\infty$. Finally, the coordinate metrics can be estimated using the coordinate mappings, $\xi=\xi(x,y,z)$, $\eta=\eta(x,y,z)$, $\zeta=\zeta(x,y,z)$.

The viscous flux terms in Eq. (1) can also be expressed by

$$\mathbf{F}_{v}=J^{-1}\begin{bmatrix}0\\ \xi_x\tau_{xx}+\xi_y\tau_{xy}+\xi_z\tau_{xz}\\ \xi_x\tau_{yx}+\xi_y\tau_{yy}+\xi_z\tau_{yz}\\ \xi_x\tau_{zx}+\xi_y\tau_{zy}+\xi_z\tau_{zz}\\ f^*\end{bmatrix}, \tag{6a}$$

$$\mathbf{G}_{v}=J^{-1}\begin{bmatrix}0\\ \eta_x\tau_{xx}+\eta_y\tau_{xy}+\eta_z\tau_{xz}\\ \eta_x\tau_{yx}+\eta_y\tau_{yy}+\eta_z\tau_{yz}\\ \eta_x\tau_{zx}+\eta_y\tau_{zy}+\eta_z\tau_{zz}\\ g^*\end{bmatrix}, \tag{6b}$$

$$\mathbf{H}_{v}=J^{-1}\begin{bmatrix}0\\ \zeta_x\tau_{xx}+\zeta_y\tau_{xy}+\zeta_z\tau_{xz}\\ \zeta_x\tau_{yx}+\zeta_y\tau_{yy}+\zeta_z\tau_{yz}\\ \zeta_x\tau_{zx}+\zeta_y\tau_{zy}+\zeta_z\tau_{zz}\\ h^*\end{bmatrix}, \tag{6c}$$

in which the components of the viscous stress tensor are,

$$\tau_{xx}=\frac{\mu}{3}\Big[4\left(\xi_x u_\xi+\eta_x u_\eta+\zeta_x u_\zeta\right)-2\left(\xi_y v_\xi+\eta_y v_\eta+\zeta_y v_\zeta\right)-2\left(\xi_z w_\xi+\eta_z w_\eta+\zeta_z w_\zeta\right)\Big], \tag{7}$$

$$\tau_{yy}=\frac{\mu}{3}\Big[-2\left(\xi_x u_\xi+\eta_x u_\eta+\zeta_x u_\zeta\right)+4\left(\xi_y v_\xi+\eta_y v_\eta+\zeta_y v_\zeta\right)-2\left(\xi_z w_\xi+\eta_z w_\eta+\zeta_z w_\zeta\right)\Big], \tag{8}$$

$$\tau_{zz}=\frac{\mu}{3}\Big[-2\left(\xi_x u_\xi+\eta_x u_\eta+\zeta_x u_\zeta\right) -2\left(\xi_y v_\xi+\eta_y v_\eta+\zeta_y v_\zeta\right) +4\left(\xi_z w_\xi+\eta_z w_\eta+\zeta_z w_\zeta\right)\Big], \tag{9}$$

$$\tau_{xy}=\tau_{yx}=\mu\Big[\xi_y u_\xi+\eta_y u_\eta+\zeta_y u_\zeta +\xi_x v_\xi+\eta_x v_\eta+\zeta_x v_\zeta\Big], \tag{10}$$

$$\tau_{xz}=\tau_{zx}=\mu\Big[\xi_z u_\xi+\eta_z u_\eta+\zeta_z u_\zeta +\xi_x w_\xi+\eta_x w_\eta+\zeta_x w_\zeta\Big], \tag{11}$$

$$\tau_{yz}=\tau_{zy}=\mu\Big[\xi_z v_\xi+\eta_z v_\eta+\zeta_z v_\zeta +\xi_y w_\xi+\eta_y w_\eta+\zeta_y w_\zeta\Big], \tag{12}$$

and

$$f^*=u\tau_{xx}+v\tau_{xy}+w\tau_{xz}+ \mu Pr^{-1}(\gamma-1)^{-1}\left(\xi_x\frac{\partial v_s^2}{\partial\xi}+\eta_x\frac{\partial v_s^2}{\partial\eta}+\zeta_x\frac{\partial v_s^2}{\partial\zeta}\right), \tag{13}$$

$$g^*=u\tau_{yx}+v\tau_{yy}+w\tau_{yz}+ \mu Pr^{-1}(\gamma-1)^{-1}\left(\xi_y\frac{\partial v_s^2}{\partial\xi}+\eta_y\frac{\partial v_s^2}{\partial\eta}+\zeta_y\frac{\partial v_s^2}{\partial\zeta}\right), \tag{14}$$

$$h^*=u\tau_{zx}+v\tau_{zy}+w\tau_{zz}+ \mu Pr^{-1}(\gamma-1)^{-1}\left(\xi_z\frac{\partial v_s^2}{\partial\xi}+\eta_z\frac{\partial v_s^2}{\partial\eta}+\zeta_z\frac{\partial v_s^2}{\partial\zeta}\right). \tag{15}$$

Here μ is the dynamic viscosity, Pr is the Prandtl number, γ is the ratio of specific heats, and v_s is the speed of sound which can be determined by $v_s^2=\gamma p/\rho$ for ideal gases. Finally, by assuming fluid as an ideal gas and employing the equation of state, we can calculate pressure as

$$P=(\gamma-1)\left(E-\frac{1}{2}\rho\left(u^2+v^2+w^2\right)\right). \tag{16}$$

It should be noted here that the Navier-Stokes equations represented in Eq. (1) can be reduced to the Euler equations by neglecting viscous flux terms.

3. NUMERICAL METHOD

3.1 Spatial Differencing

We employed the high-order compact finite difference scheme proposed by Lele (1992) to discretize the spatial derivatives of the fluid flow governing equations. Compact schemes have the advantage of providing high-accurate discretization of first- and second-order spatial derivatives, while they require short-sized stencils. Given the values of a function on a set of grid points, the compact finite-difference approximation to the derivative of the function is implicitly expressed as a linear combination of the given function values. For instance, the generalized form of first derivatives can be described for a general function $f(x)$ as

$$\beta f'_{i-2}+\alpha f'_{i-1}+f'_i+\alpha f'_{i+1}+\beta f'_{i+2}= a\frac{f_{i+1}-f_{i-1}}{2h}+b\frac{f_{i+2}-f_{i-2}}{4h}+c\frac{f_{i+3}-f_{i-3}}{6h}, \tag{17}$$

where f'_i denotes derivative of f at node i, h refers to the grid spacing difference, and the coefficients α, β, a, b, c can determine the spatial characteristics of the algorithm. The relation between coefficients α, β and a, b, c can be derived by employing Taylor expansion. Moreover, in order to keep the method non-dissipative, the stencil and the weighted factors are set to be symmetric. We employed the fourth-order compact finite-difference formulations as our spatial differencing scheme by setting $\alpha=1/4$, $\beta=0$, $a=3/4$, $b=0$, and $c=-3/4$ in Eq. (17) so that

$$f'_{i+1}+4f'_i+f'_{i-1}=\frac{3}{h}(f_{i+1}-f_{i-1})+O\left(h^4\right). \tag{18}$$

The above formulations cannot be directly implemented to the near boundary regions since it extends to the grid points beyond the computational domain. For points close to the boundaries, we also considered high-order forward and backward compact schemes to preserve the tridiagonal form of the equations. The following formulations, therefore, were used to treat the physical boundary points at nodes $i=1$ and $i=IL$, respectively,

$$f'_1+3f'_2=\frac{1}{6h}(-17f_1+9f_2+9f_3-f_4) +O(h^4), \tag{19}$$

$$f'_{IL-1}+f'_{IL}=\frac{1}{6h}(17f_{IL}-9f_{IL-1} -9f_{IL-2}+f_{IL-3})+O(h^4). \tag{20}$$

This fourth-order accurate scheme near the boundaries allowed us to retain the accuracy of the numerical solution over the entire computational domain.

3.2 Temporal Discretization

The equations are integrated in time following the implicit FDM developed by Beam and Warming (1976), basically for the numerical solution of nonlinear hyperbolic equations. To this end, we extended the implicit Beam–Warming algorithm to 3D viscous fluid flow equations. The equations and the numerical discretization are explained in detail in the following.

The algorithm is implicit, second–order time–accurate, and in a spatially factored form wherein a

fourth-order compact scheme (Eq. (18)) is implemented. Using the trapezoidal formula (Beam and Warming, 1976), we can express the time–differencing equation as

$$\mathbf{U}^{n+1}=\mathbf{U}^{n}+\frac{\Delta t}{2}\left[\left(\frac{\partial \mathbf{U}}{\partial t}\right)^{n}+\left(\frac{\partial \mathbf{U}}{\partial t}\right)^{n+1}\right]+O\left(\Delta t^{3}\right), \tag{21}$$

in which U^{n+1} is the updated value of U^{n} at the iteration $n+1$ and Δt is the time step size. By substituting Eq.1 into the above equation, we have,

$$\begin{aligned}\mathbf{U}^{n+1}=\mathbf{U}^{n}-\frac{\Delta t}{2}\Bigg[&\left(\frac{\partial}{\partial \xi}\left(\mathbf{F}-\frac{1}{Re}\mathbf{F}_{\nu}\right)+\frac{\partial}{\partial \eta}\left(\mathbf{G}-\frac{1}{Re}\mathbf{G}_{\nu}\right)+\frac{\partial}{\partial \zeta}\left(\mathbf{H}-\frac{1}{Re}\mathbf{H}_{\nu}\right)\right)^{n}\\&+\left(\frac{\partial}{\partial \xi}\left(\mathbf{F}-\frac{1}{Re}\mathbf{F}_{\nu}\right)+\frac{\partial}{\partial \eta}\left(\mathbf{G}-\frac{1}{Re}\mathbf{G}_{\nu}\right)+\frac{\partial}{\partial \zeta}\left(\mathbf{H}-\frac{1}{Re}\mathbf{H}_{\nu}\right)\right)^{n+1}\Bigg]+O\left(\Delta t^{3}\right)\end{aligned} \tag{22}$$

A local Taylor expansion about U^{n} leads to a linear relation between flux vector F^{n+1} and variable vector U^{n+1} such that,

$$\mathrm{F}^{n+1}=\mathrm{F}^{n}+\mathrm{A}^{n}\left(\mathrm{U}^{n+1}-\mathrm{U}^{n}\right)+\mathrm{O}\left(\Delta t^{2}\right), \tag{23}$$

where A is the Jacobian matrix,

$$\mathbf{A}^{n}=\frac{\partial \mathbf{F}^{n}}{\partial \mathbf{U}^{n}}. \tag{24}$$

Similar linearization was also applied to other flux terms G, H, F_{ν}, G_{ν}, and H_{ν}. Moreover, the Alternating-Direction-Implicit (ADI) method (see Douglas and Gunn, 1964) and fractional step algorithm (see Janenko, 1971) were next applied to Eq. (22) to take advantage of efficient multi-dimensional implicit algorithms. Equation (22) can be therefore reduced to,

$$\begin{aligned}&\left(\left[\mathbf{I}+\frac{\Delta t}{2}\frac{\partial}{\partial \xi}\left(\mathbf{A}^{n}-\frac{1}{Re}\mathbf{A}_{\nu}^{n}\right)\right]\right.\\&\left[\mathbf{I}+\frac{\Delta t}{2}\frac{\partial}{\partial \eta}\left(\mathbf{B}^{n}-\frac{1}{Re}\mathbf{B}_{\nu}^{n}\right)\right]\\&\left.\left[\mathbf{I}+\frac{\Delta t}{2}\frac{\partial}{\partial \zeta}\left(\mathbf{C}^{n}-\frac{1}{Re}\mathbf{C}_{\nu}^{n}\right)\right]\right)\mathbf{U}^{n+1}=RHS,\end{aligned} \tag{25}$$

Where,

$$\begin{aligned}RHS=&\left(\left[\mathbf{I}+\frac{\Delta t}{2}\frac{\partial}{\partial \xi}\left(\mathbf{A}^{n}-\frac{1}{Re}\mathbf{A}_{\nu}^{n}\right)\right]\right.\\&\left[\mathbf{I}+\frac{\Delta t}{2}\frac{\partial}{\partial \eta}\left(\mathbf{B}^{n}-\frac{1}{Re}\mathbf{B}_{\nu}^{n}\right)\right]\\&\left.\left[\mathbf{I}+\frac{\Delta t}{2}\frac{\partial}{\partial \zeta}\left(\mathbf{C}^{n}-\frac{1}{Re}\mathbf{C}_{\nu}^{n}\right)\right]\right)\mathbf{U}^{n}\\&-\Delta t\left[\frac{\partial}{\partial \xi}\left(\mathbf{F}^{n}-\frac{1}{Re}\mathbf{F}_{\nu}^{n}\right)+\frac{\partial}{\partial \eta}\left(\mathbf{G}^{n}-\frac{1}{Re}\mathbf{G}_{\nu}^{n}\right)\right.\\&\left.+\frac{\partial}{\partial \zeta}\left(\mathbf{H}^{n}-\frac{1}{Re}\mathbf{H}_{\nu}^{n}\right)\right],\end{aligned} \tag{26}$$

I is the identity matrix, and Jacobian matrices are defined as follows,

$$\mathbf{B}^{n}=\frac{\partial \mathbf{G}^{n}}{\partial \mathbf{U}^{n}},\quad \mathrm{C}^{n}=\frac{\partial \mathbf{H}^{n}}{\partial \mathbf{U}^{n}}, \tag{27}$$

and similarly,

$$\mathbf{A}_{\nu}^{n}=\frac{\partial \mathbf{F}_{\nu}^{n}}{\partial \mathbf{U}^{n}},\quad \mathbf{B}_{\nu}^{n}=\frac{\partial \mathbf{G}_{\nu}^{n}}{\partial \mathbf{U}^{n}},\quad \mathbf{C}_{\nu}^{n}=\frac{\partial \mathbf{H}_{\nu}^{n}}{\partial \mathbf{U}^{n}}. \tag{28}$$

Through the above-mentioned procedure, the complexity of the problem is reduced from an immense matrix inversion (see Eq. (22) to a series of tridiagonal matrix inversion problems for which efficient solution algorithms exist. In order to solve Eq. (25), three one-dimensional sweeps are utilized,

$$\left[\mathbf{I}+\frac{\Delta t}{2}\frac{\partial}{\partial \xi}\left(\mathbf{A}^{n}-\frac{1}{Re}\mathbf{A}_{\nu}^{n}\right)\right]\Delta \mathbf{U}^{**}=RHS, \tag{29a}$$

$$\left[\mathbf{I}+\frac{\Delta t}{2}\frac{\partial}{\partial \eta}\left(\mathbf{B}^{n}-\frac{1}{Re}\mathbf{B}_{\nu}^{n}\right)\right]\Delta \mathbf{U}^{*}=\Delta \mathbf{U}^{**}, \tag{29b}$$

$$\left[\mathbf{I}+\frac{\Delta t}{2}\frac{\partial}{\partial \zeta}\left(\mathbf{C}^{n}-\frac{1}{Re}\mathbf{C}_{\nu}^{n}\right)\right]\Delta \mathbf{U}^{n}=\Delta \mathbf{U}^{*}, \tag{29c}$$

in which $\Delta \mathrm{U}^{**}$ and $\Delta \mathrm{U}^{*}$ are mediator variables, $\Delta \mathrm{U}^{n}=\mathrm{U}^{n+1}-\mathrm{U}^{n}$, and *RHS* is defined in Eq. (26). Equations (29a) to (29c) are sweeps in the ξ, η, and ζ directions, respectively. By substituting Eq. (18) with first-order derivatives into Eqs. (29)a to Eqs. (29)c, we reach to the system of equations below,

$$\begin{aligned}&\left(-\frac{\Delta t}{2}\left(\mathbf{A}_{i-1}-\frac{1}{Re}\mathbf{A}_{\nu,(i-1)}\right)+\frac{1}{6}\right)\Delta \mathbf{U}_{i-1}^{**}\\&+\frac{2}{3}\Delta \mathbf{U}_{i}^{**}\\&+\left(\frac{\Delta t}{2}\left(\mathbf{A}_{i+1}-\frac{1}{Re}\mathbf{A}_{\nu,(i+1)}\right)+\frac{1}{6}\right)\Delta \mathbf{U}_{i+1}^{**}\\&=RHS,\end{aligned} \tag{30a}$$

$$\left(-\frac{\Delta t}{2}\left(\mathbf{B}_{j-1}-\frac{1}{Re}\mathbf{B}_{v,(j-1)}\right)+\frac{1}{6}\right)\Delta\mathbf{U}^{*}_{j-1}+\frac{2}{3}\Delta\mathbf{U}^{*}_{j}+\left(\frac{\Delta t}{2}\left(\mathbf{B}_{j+1}-\frac{1}{Re}\mathbf{B}_{v,(j+1)}\right)+\frac{1}{6}\right)\Delta\mathbf{U}^{*}_{j+1}=\frac{1}{6}\left(\Delta\mathbf{U}^{**}_{j-1}+4\Delta\mathbf{U}^{**}_{j}+\Delta\mathbf{U}^{**}_{j+1}\right), \quad (30b)$$

$$\left(-\frac{\Delta t}{2}\left(\mathbf{C}_{k-1}-\frac{1}{Re}\mathbf{C}_{v,(k-1)}\right)+\frac{1}{6}\right)\Delta\mathbf{U}^{n}_{k-1}+\frac{2}{3}\Delta\mathbf{U}^{n}_{k}+\left(\frac{\Delta t}{2}\left(\mathbf{C}_{k+1}-\frac{1}{Re}\mathbf{C}_{v,(k+1)}\right)+\frac{1}{6}\right)\Delta\mathbf{U}^{n}_{k+1}=\frac{1}{6}\left(\Delta\mathbf{U}^{*}_{k-1}+4\Delta\mathbf{U}^{*}_{k}+\Delta\mathbf{U}^{*}_{k+1}\right), \quad (30c)$$

in which, *RHS* again refers to the right-hand side of Eq. (25) (see Eq. (26)). Here, the updated value of the variable vector $\mathbf{U}^{n+1}$ is obtained through calculating $\Delta\mathbf{U}^{n} = \mathbf{U}^{n+1} - \mathbf{U}^{n}$ from Eq. (30c). The above expressions represent a system of tridiagonal matrix inversion problem solved by Thomas's algorithm.

3.3 Spatial Filtering

The primary source of computational uncertainties arises from mesh nonuniformities, rough boundary conditions, and nonlinear behavior of the fluid flow. In the present study, however, we are mainly concerned with the inviscid nonlinear terms in the governing equations being the main source of instabilities and irregularities. Such instabilities, in fact, continuously generate unrestricted high-frequency wave modes. In order to smooth the generation of high-frequency wave modes, a high-order compact spatial filtering (e.g., Zhang *et al.* 2004) is implemented in the current numerical approach. The implicit filter applied to the solution vector can be expressed as,

$$\alpha_f\hat{\phi}_{i-1}+\hat{\phi}_i+\alpha_f\hat{\phi}_{i+1}=\sum_{n=0}^{N}\frac{a_n}{2}\left(\phi_{i+n}+\phi_{i-n}\right), \quad (31)$$

where $\hat{\phi}_i$ is the filtered function of ϕ_i at grid point i, α_f is the coefficient of implicit terms normally varies between $0.3<\alpha_f<0.5$, a_n is the coefficient of explicit terms for different orders of filter, and $2\times N$ is the order of the filter. Higher values of α_f result in less dissipative filters through filtering higher wavenumber modes. The coefficients a_n can be computed using Taylor expansion for different orders of the filter. For a sixth-order filter, we have,

$$\begin{aligned} a_0 &= \frac{11}{16}+\frac{5}{8}\alpha_f, \\ a_1 &= \frac{15}{32}+\frac{17}{16}\alpha_f. \\ a_2 &= -\frac{3}{16}+\frac{3}{8}\alpha_f, \\ a_3 &= -\frac{1}{32}-\frac{1}{16}\alpha_f, \end{aligned} \quad (32)$$

with $\alpha_f = 0.4$. The filter operator (see Eq. (31)) was applied to the variable vector U^{n+1} obtained from Eq.30 after each time step, and subsequently, calculated using tridiagonal matrix solvers (i.e. Thomas's algorithm). Moreover, for the boundary points, sixth-order forward and backward filtering was again used as following

$$\alpha_f\hat{\phi}_{i-1}+\hat{\phi}_i+\hat{\phi}_f\phi_{i+1}=\sum_{n=1}^{7}a_{n,i}\phi_n \quad (i=2,3) \quad (33a)$$

$$\alpha_f\hat{\phi}_{i-1}+\hat{\phi}_i+\alpha_f\hat{\phi}_{i+1}=\sum_{n=0}^{6}a_{IL-n,i}\phi_{IL-n} \quad (i=IL-2, IL-1) \quad (33b)$$

where the coefficients of right-hand side of the above equations can be found in Gaitonde and Visbal (2000). We note here that the values at points $i=1, IL$ were explicitly determined through the boundary conditions and were not filtered. Hence, the tridiagonal structure of the filtering was completely preserved. It is also worth mentioning that such low-pass high-order filter restores the advantages of high-order approaches.

4. INTERFACE TREATMENT IN MULTI-BLOCK CALCULATIONS

As noted, adopting multi-block-type approaches appears to be necessary for numerical simulations of problems with complex geometries. The primary challenge, however, is the treatment of the block interface between subdomains. In the present work, a conservative interface boundary treatment is proposed to implement a high-order compact finite-difference method on multi-block subdomains, which is not only accurate but suitable for the massively parallel computations of turbulent flows. The one-dimensional, simplified representation of the block-interface strategy in a multi-block approach is schematically demonstrated in Fig. (1).To explain the communication between different blocks, we assume two neighboring blocks, i.e. Block 1 and Block 2, with N grid points in each block. Here, the N^{th} node of Block 1 and the first node of Block 2 are the shared nodes, and the grid points $i=2$ to $i=N-1$ are the internal nodes. For internal nodes in each block, the governing equations presented in previous sections are solved, while we apply the known values of the governing equations computed from neighboring blocks for the boundary

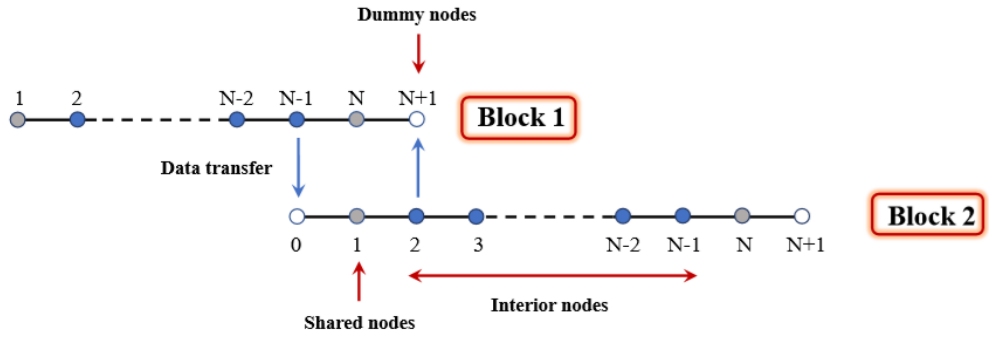

Fig. 1. Schematic representation of the block-interface strategy and data transfer between two neighboring blocks in the current multi-block approach applied to the implicit fourth-order compact finite-difference method. The internal, dummy, and shared nodes are also indicated by blue, white, and grey (grid) points, respectively. For internal nodes on each block, the governing equations are solved, while the known values of the governing equations computed from neighboring blocks are applied for boundary points.

points (i.e. $i=1$ and $i=N$). This allows us to solve the governing equations directly on the block interfaces and, consequently, to preserve the conservation laws.

For solving governing equations at the node N of Block 1 (see Fig. 1), Eqs. (30) are applied in such a way that the (i +1) terms in Eq. (30a) are assumed to be known values obtained from the neighboring block. Equations (30a) to (30c) are then reduced to

$$\left(-\frac{\Delta t}{2}\left(\mathbf{A}_{i-1}-\frac{1}{Re}\mathbf{A}_{\nu,(i-1)}\right)+\frac{1}{6}\right)\Delta\mathbf{U}_{i-1}^{**} +\frac{2}{3}\Delta\mathbf{U}_{i}^{**}=RHS^{*}, \tag{34a}$$

$$\left(-\frac{\Delta t}{2}\left(\mathbf{B}_{j-1}-\frac{1}{Re}\mathbf{B}_{\nu,(j-1)}\right)+\frac{1}{6}\right)\Delta\mathbf{U}_{j-1}^{*} +\frac{2}{3}\Delta\mathbf{U}_{j}^{*}n =\frac{1}{6}\left(\Delta\mathbf{U}_{j-1}^{**}+4\Delta\mathbf{U}_{j}^{**}+\Delta\mathbf{U}_{j+1}^{**}\right) -\left(\frac{\Delta t}{2}\left(\mathbf{B}_{j+1}-\frac{1}{Re}\mathbf{B}_{\nu,(j+1)}\right)+\frac{1}{6}\right)\Delta\mathbf{U}_{j+1}^{*}, \tag{34b}$$

$$\left(-\frac{\Delta t}{2}\left(\mathbf{C}_{k-1}-\frac{1}{Re}\mathbf{C}_{\nu,(k-1)}\right)+\frac{1}{6}\right)\Delta\mathbf{U}_{k-1}^{n} +\frac{2}{3}\Delta\mathbf{U}_{k}^{n} =\frac{1}{6}\left(\Delta\mathbf{U}_{k-1}^{*}+4\Delta\mathbf{U}_{k}^{*}+\Delta\mathbf{U}_{k+1}^{*}\right) -\left(\frac{\Delta t}{2}\left(\mathbf{C}_{k+1}-\frac{1}{Re}\mathbf{C}_{\nu,(k+1)}\right)+\frac{1}{6}\right)\Delta\mathbf{U}_{k+1}^{n}, \tag{34c}$$

in which

$$RHS^{*}=RHS -\left(\frac{\Delta t}{2}\left(\mathbf{A}_{i+1}-\frac{1}{Re}\mathbf{A}_{\nu,(i+1)}\right)+\frac{1}{6}\right)\Delta\mathbf{U}_{i+1}^{**}.$$

Similarly, for solving governing equations at the first node of Block 2, the (i−1) terms in Eq. (30a) are assumed to be known values calculated from the neighboring subdomain, i.e. Block 1. Equations (30a) to (30c) can be then expressed by

$$\frac{2}{3}\Delta\mathbf{U}_{i}^{**} +\left(\frac{\Delta t}{2}\left(\mathbf{A}_{i+1}-\frac{1}{Re}\mathbf{A}_{\nu,(i+1)}\right)+\frac{1}{6}\right)\Delta\mathbf{U}_{i+1}^{**} =RHS^{**}, \tag{35a}$$

$$\frac{2}{3}\Delta\mathbf{U}_{j}^{*} +\left(\frac{\Delta t}{2}\left(\mathbf{B}_{j+1}-\frac{1}{Re}\mathbf{B}_{\nu,(j+1)}\right)+\frac{1}{6}\right)\Delta\mathbf{U}_{j+1}^{*} =\frac{1}{6}\left(\Delta\mathbf{U}_{j-1}^{**}+4\Delta\mathbf{U}_{j}^{**}+\Delta\mathbf{U}_{j+1}^{**}\right) -\left(-\frac{\Delta t}{2}\left(\mathbf{B}_{j-1}-\frac{1}{Re}\mathbf{B}_{\nu,(j-1)}\right)+\frac{1}{6}\right)\Delta\mathbf{U}_{j-1}^{*}, \tag{35b}$$

$$\frac{2}{3}\Delta\mathbf{U}_{k}^{n} +\left(\frac{\Delta t}{2}\left(\mathbf{C}_{k+1}-\frac{1}{Re}\mathbf{C}_{\nu,(k+1)}\right)+\frac{1}{6}\right)\Delta\mathbf{U}_{k+1}^{n} =\frac{1}{6}\left(\Delta\mathbf{U}_{k-1}^{*}+4\Delta\mathbf{U}_{k}^{*}+\Delta\mathbf{U}_{k+1}^{*}\right) -\left(-\frac{\Delta t}{2}\left(\mathbf{C}_{k-1}-\frac{1}{Re}\mathbf{C}_{\nu,(k-1)}\right)+\frac{1}{6}\right)\Delta\mathbf{U}_{k-1}^{n}, \tag{35c}$$

in which

$$RHS^{**}=RHS -\left(-\frac{\Delta t}{2}\left(\mathbf{A}_{i-1}-\frac{1}{Re}\mathbf{A}_{\nu,(i-1)}\right)+\frac{1}{6}\right)\Delta\mathbf{U}_{i-1}^{**}.$$

In comparison with a single block solution, the structure and accuracy of the multi-block compact method are conserved through block interfaces. The benefit of the present interface method compared to previous studies that, for example, developed multi-block compact finite-difference solvers on overlapping blocks, is that our conservative

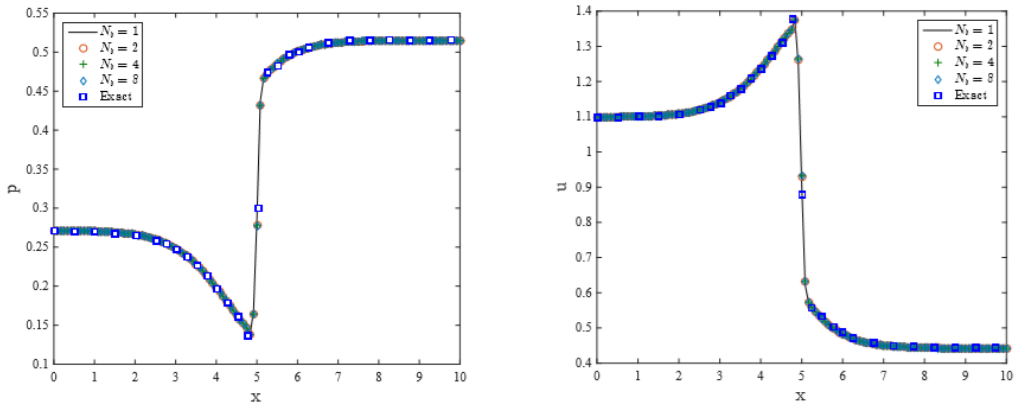

(a) (b)

Fig. 2. (a) Pressure and (b) velocity profiles of the supersonic flow inside the Shubin nozzle obtained by the fourth-order compact finite-difference scheme using the multi-block solver with N_b = 1, 2, 4, and 8. The computational results are also compared with the exact solution (see, for example, Shubin *et al.* 1981).

approach can deal with jumps and shocks passing through the block interfaces. Moreover, the method does not require any flow sensors or tuning parameters. The proposed block interface condition can be further applied to complex geometries with additional high-order interpolation methods in overset-grid methodologies.

5. RESULTS AND DISCUSSIONS

5.1 One-Dimensional flow Inside a Nozzle

In order to examine the capability and performance of the presented multi-block solver on accurately capturing shock waves, we first calculate a quasi-one-dimensional supersonic flow with normal shock inside the Shubin nozzle (see Shubin *et al.* 1981).

The cross-sectional area of the nozzle is of the form,

$$S(x) = 1.398 + 0.347\left[\tanh\left(0.8x - 0.4\right)\right]. \qquad (36)$$

The 1D Euler equations are solved on the domain $x \in [0,10]$ with $\Delta x = 0.1$ and $\gamma = 1.4$. The supersonic condition was specified at the inflow, and the pressure at the outflow was set in such a way that a normal shock happened at the location of $x = 5$. The inflow and outflow conditions are summarized in Table.1. It should also be noted here that the Euler equations can be obtained by ignoring viscous flux terms in Navier-Stokes equations (see Eq. (1)).

Figure 2 illustrates the pressure and velocity distributions along the nozzle length calculated in the multi-block solver for different block numbers of N_b = 1, 2, 4, and 8. The exact analytical solution to the problem is also presented in this figure for comparison purposes. It can be observed that the result of the multi-block fourth-order compact method agrees quite well with the exact solution (see, for example, Shubin *et al.* 1981).

Table 1 Inflow and outflow conditions off low inside the nozzle

Inflow condition	Outflow condition
$\rho_{in} = 0.0500826$ $p_{in} = 0.2712900$ $u_{in} = 1.0991840$ $Ma = 1.2622140$	$p_{out} = 0.5156000$

The multi-block solver developed in the present study performs practically in the same fashion as the single-block solver (N_b = 1) in capturing the shock; the profiles are barely distinguishable from the single-block solution. It is worth mentioning here that the multi-block solution is conservative and stable when the block interface meets the shock location and accurately captures the jump.

Further, in order to evaluate the accuracy of the multi-block high-order method, a $L2$-norm error is calculated based on the pressure values,

$$\textbf{Error(L2)} = \sqrt{\int (p - p_e)^2 dx} \qquad (37)$$

where p_e is the pressure from the exact solution. Figure 3 shows that both single- and multiblock compact finite–difference schemes preserve the fourth–order accuracy of the compact finite–difference method.

5.2 Two-Dimensional Inviscid flow over a Circular Bump

The flow over a bump is a solid examination for assessing the capability of numerical algorithms (e.g., Favini *et al.* 1996; Darwish *et al.* 2004). Therefore, we consider the supersonic inviscid flow over a circular bump to evaluate the stability and accuracy of the implicit fourth-order compact solver in 2D problems. The proposed multi-block strategy

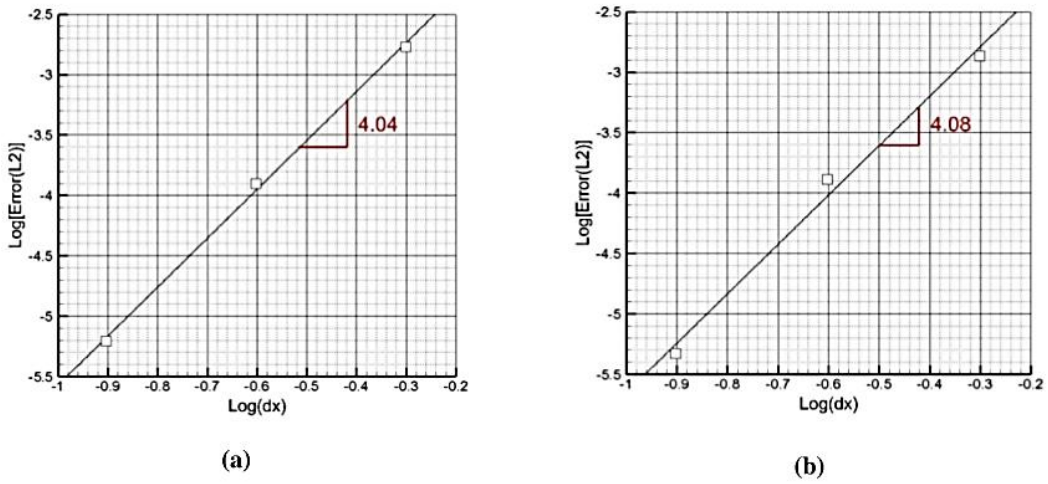

Fig. 3. Accuracy estimation of the compact finite-difference method for the supersonic flow inside the Shubin nozzle: (a) single-block solution, (b) multi-block solver with $N_b = 4$. The corresponding error of different grid resolutions is indicated by square symbols. The solid line is also the best linear fit to the data.

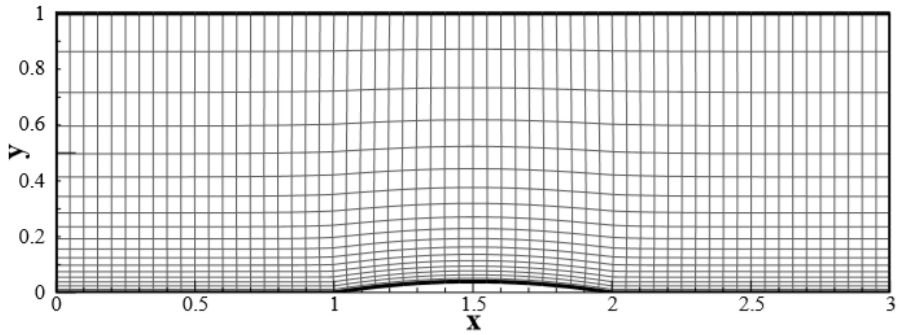

Fig. 4. Schematic representation of the grid generated over a circular bump with a thickness-to-chord ratio of 4% using the methodology proposed by Steger and Sorenson (1979) for which Eqs. (39) were solved.

is further assessed in a 2D domain decomposition. To this end, the 2D Euler equations with $Ma = 1.4$ and $\gamma = 1.4$ are solved on the domain $x \in [0,3]$ and $y \in [0,1]$ with $\Delta x = 0.375$ and $\Delta y = 0.05$ which is corresponding to $N_x = 80$ and $N_y = 20$ grid points in x and y directions, respectively. The thickness-to-chord ratio of the circular bump is 4%, and it is located at the middle of a rectangular channel which is $3L_c$ long and $1L_c$ wide, where L_c is the bump chord. To obtain body-fitted grid points, a system of elliptic partial differential equations (see Thompson *et al.* 1974; Steger and Sorenson, 1979; Sorenson, 1982) is solved,

$$\begin{aligned} \xi_{xx} + \xi_{yy} &= P(\xi,\eta), \\ \eta_{xx} + \eta_{yy} &= Q(\xi,\eta), \end{aligned} \tag{38}$$

in which P and Q control the clustering and orthogonality of grid points near the boundaries. In the physical space (ξ,η), these equations are written as

$$\begin{aligned} \alpha x_{\xi\xi} - 2\beta x_{\xi\eta} + \gamma x_{\eta\eta} &= -J^2(Px_\xi + Qx_\eta), \\ \alpha y_{\xi\xi} - 2\beta y_{\xi\eta} + \gamma y_{\eta\eta} &= -J^2(Py_\xi + Qy_\eta), \end{aligned} \tag{39}$$

where J is the transformed Jacobian defined by $J = x_\xi y_\eta - x_\eta y_\xi$ and

$$\begin{aligned} \alpha &= x_\eta^2 + y_\eta^2, \\ \beta &= x_\eta x_\xi + y_\eta y_\xi, \\ \gamma &= x_\xi^2 + y_\xi^2. \end{aligned} \tag{40}$$

Figure 4 depicts the schematic of the grid generated over the circular bump for which the set of Eqs. (39) were solved. The estimated distribution of the pressure field on the lower wall is also shown in Fig. 5. From the pressure contours, it can be noted that shock waves are formed at the leading and trailing edges of the bump. The leading-edge shock wave above the bump is developed across the channel and reflected upon reaching the upper boundary. This reflected shock wave interacts with the trailing-edge

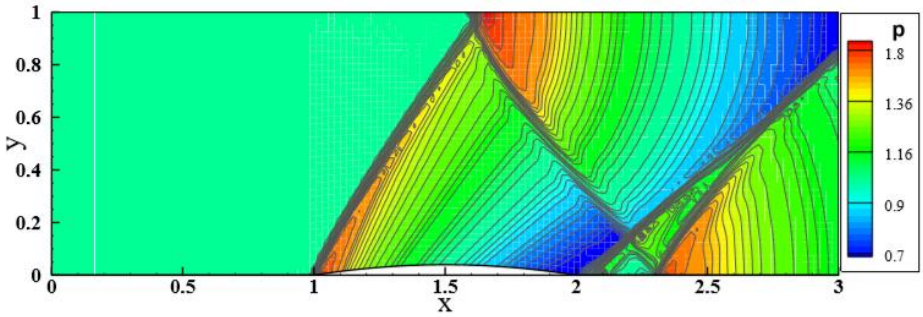

Fig. 5. Pressure filed of supersonic flow with *Ma* = 1.4 over a circular bump with a thickness-to-chord ratio of 4%. All flow discontinuities were accurately captured.

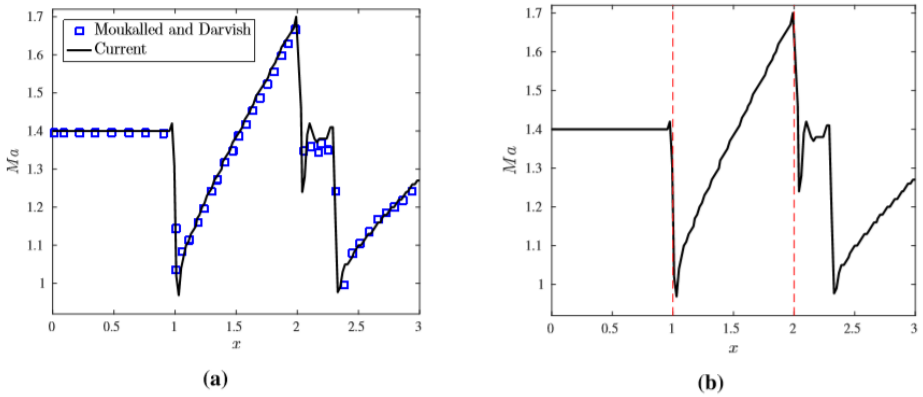

Fig. 6. Distributions of Mach number of a supersonic flow with *Ma* = 1.4 over a 4% circular bump and along the lower wall: (a) comparison of the current high-order implicit solver with the results obtained by Moukalled and Darwish (2001), (b) comparison of the current multi-block solution (N_b = 3) with the single-block solver. Dashed red lines indicate the block-interfaces in the multi-block solution.

shock wave, impinges, and hits the lower boundary where it is again reflected. This is in complete agreement with previous results of, for example, Hendriana and Bathe (2000), Darwish *et al*. (2004), and Yang *et al*. (2016). We also note here that all the shocks were accurately resolved.

The distribution of Mach number over the bump and along the lower wall is next shown in Fig. 6a. The results of the fourth-order implicit compact scheme are also compared and in complete agreement with those obtained by Moukalled and Darwish (2001). It can also be observed from Fig. 6a that, with an inlet Mach number of 1.4 and the bump geometry, the flow remained supersonic at the outlet. Moreover, the results of the proposed multi-block solver with N_b = 3 are exhibited in Fig. 6b, presenting roughly the same accuracy as the single block solution. This is partially important when block interfaces intersect at the shock location, demonstrating the capability of the proposed multi-block strategy to accurately resolve flow discontinuities over complex geometry.

5.3 Three–Dimensional Compressible Viscous

In order to examine the framework proposed in the current work in a more physically complicated case, the three-dimensional transonic viscous flow around a NACA 0012 airfoil is solved using the high-order compact scheme. The three-dimensional Navier-Stokes equations with an inlet Mach number of $Ma = 0.85$, a Reynolds number of $Re = 500$, and an angle of attack of $\alpha = 0^{\circ}$ are solved on the computational domain presented in Fig. (7). This laminar flow case over the NACA 0012 airfoil (see Yousefi and Razeghi, 2018) is frequently used to assess the accuracy, stability, and convergence of numerical algorithms for solving the Navier-Stokes equations. The C-type computational grid with single- and multi-block structures, which is shown in Fig.8, was generated using the method proposed by Steger and Sorenson (1979). The computational domain was considered large enough to not affect the flow field around the airfoil by the far-field boundaries. The grid extends from 5C upstream (left boundary) to 7C downstream (right boundary), and the upper and lower boundaries extend 6C from the airfoil profile. The grid also extends 2C in the spanwise direction. Moreover, the grid with multizonal blocks contains 72 blocks in total. Finally, the structured mesh system employed in the current work consists of $N_x = 129$, $N_y = 37$, and $N_z = 37$ grid points in streamwise, normal, and spanwise directions, respectively. Also, the grid is uniform in the z direction.

The distributions of pressure and shear stresses on the airfoil surface are of great importance for assessing the numerical accuracy and have remained

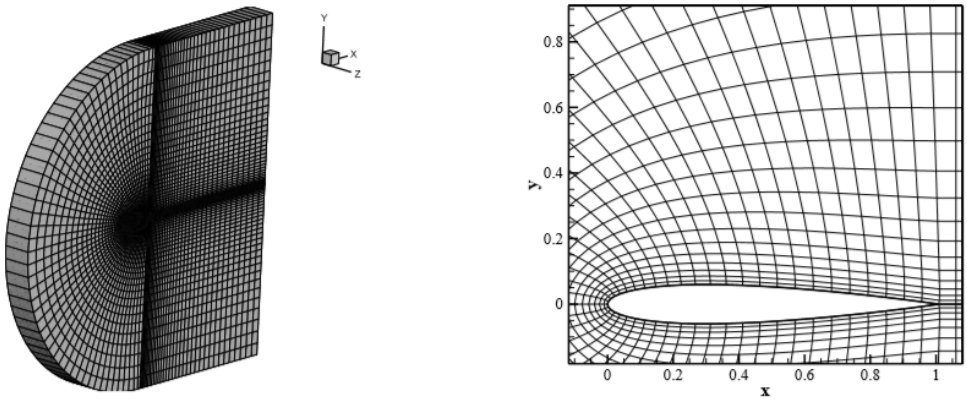

Fig. 7. Schematic representation of the computational domain and grid around the NACA 0012 airfoil. (a) Three-dimensional view and (b) close-up view of the grid around the airfoil in *x*−y plane. The structured mesh system consists of N_x = 129, N_y = 37, and N_z = 37 grid points.

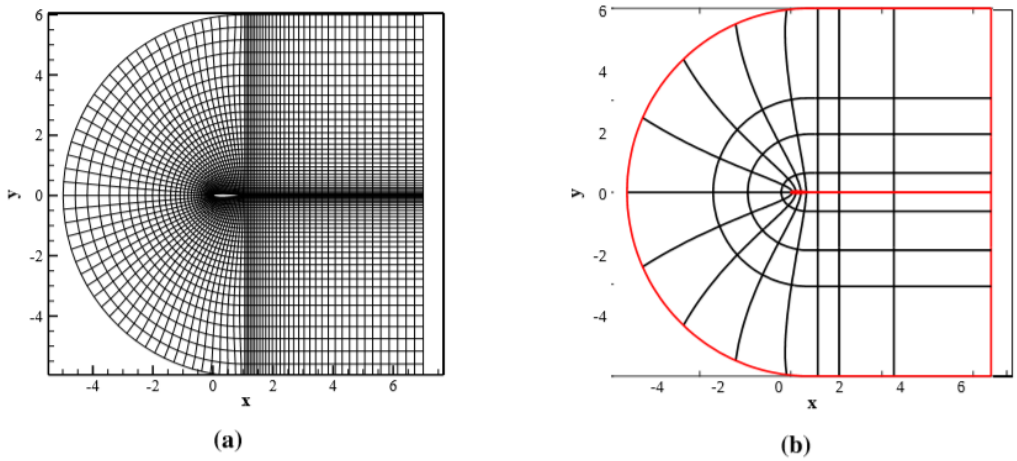

Fig. 8. Sketch of the two-dimensional view (in *x* −y plane) of the (a) single-block and (b) multi-block computational domain around the NACA 0012 airfoil. The multi-block grid consists of a total of 72 blocks. Here, solid red lines indicate the computational boundaries and solid black lines represent the block interface.

a rather primary challenge. The pressure distribution can usually be expressed in terms of the pressure coefficient, defined as,

$$C_p = \frac{p - p_\infty}{\frac{1}{2}\rho u_\infty^2}, \tag{41}$$

in which p is the static pressure, p_∞ is the free-stream pressure, ρ is the free-stream density, and u_∞ is the free-stream velocity. Therefore, C_p is the difference between local and free-stream static pressures normalized by the free-stream dynamic pressure. Figure 9a represents the distribution of the pressure coefficient on the surface of the airfoil. The pressure coefficient is presenting a smooth variation (without a suction peak) over the airfoil profile.

The pressure coefficient rises rapidly and then recovers to small positive values near the trailing edge. The results of the high-order implicit compact FDM for the pressure coefficient are also compared with the reference solution of the GAMM-Workshop (see Bristeau *et al.* 1987) in Fig. 9a. The present numerical results are quantitatively in agreement with those obtained in the reference solution.

Similarly, the skin friction coefficient, c_f, can be defined by,

$$c_f = \frac{\tau_w}{\frac{1}{2}\rho u_\infty^2}, \tag{42}$$

where τ_w is the local wall shear stress. The wall distribution of the skin friction coefficient over the airfoil is presented in Fig. 9b. Immediately after the

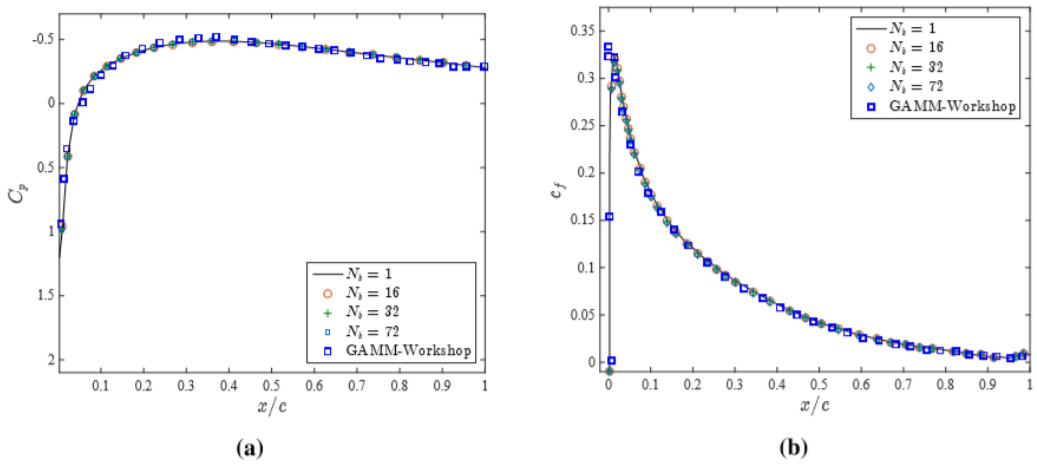

(a) (b)

Fig. 9. A comparison of the present multi-block high-order compact solution with the results of GAMM Workshop (see Bristeau *et al.* 1987) for the flow around a NACA 0012 airfoil with *Ma* = 0.85 and *Re* = 500. (a) Pressure coefficient profile and (b) friction coefficient profile.

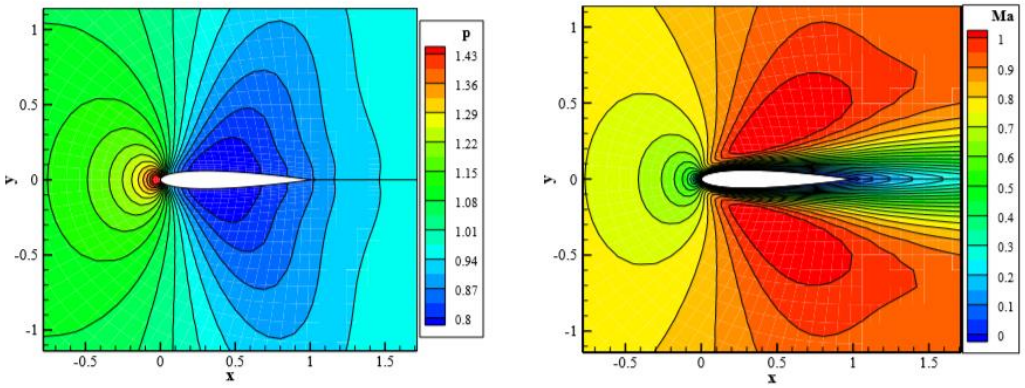

(a) (b)

Fig. 10. Flow field around the NACA 0012 airfoil with *Ma* = 0.85 and *Re* = 500. (a) Pressure contour and (b) Mach number contour. Here, both counters of the pressure and Mach number present symmetric pattern.

stagnation point, the skin friction coefficient is amplified.

It then uniformly decreases and returns to its initial value near the trailing edge. It should also be noted that there exist no drastic variations in c_f (as expected) at the trailing edge at an angle of attack of zero degrees. The current results for the skin friction coefficient are also compared against the results of the GAMM-Workshop (see Bristeau *et al.* 1987), Furthermore, as it can be observed from Figs. 9a and 9b , the excellent agreement between the multi-block and reference results validates the accuracy of the multi-block strategy proposed in the current study.

The contours of pressure and Mach number over the airfoil at the middle of the domain ($z = 0$) are next shown in Fig.10.The contour of the static pressure over the airfoil (see Fig.10a)is symmetric with respect to the upper and lower surfaces where the stagnation point precisely locates at the nose of the airfoil. Moreover, from the pressure contour, it can be observed that the region of high-pressure is located at the stagnation point, while the regions of low-pressure occur on the lower and upper surfaces of the airfoil. The contour map for the Mach number is also represented in Fig. 10b. The airfoil experiences a zero value of Mach number at the stagnation point on the leading edge. Far from the lower and upper airfoil surfaces, the Mach number increases to its peak value. At a zero-degree angle of attack, similar to the pressure counters, the counters of Mach number present symmetric pattern (almost identical) about the airfoil chord.

6. CONCLUSIONS

In the current work, we proposed a conservative block-interface boundary treatment for high-order compact finite-difference schemes with multi-block subdomains to solve compressible fluid flow problems. The approach is based on solving the

governing equations directly on the block interfaces, and thus, preserving the conservation laws. Moreover, the proposed method is easy to implement, and that avoids further complexities in numerical algorithms.

The capability of the block-interface approach in capturing shocks and discontinuities is assessed in detail by solving several benchmark test cases, including 1D fluid flow inside a Shubin nozzle, 2D channel flow with a bump, and 3D flow around a NACA 0012 airfoil. The method presented an excellent performance for 1D and 2D problems, particularly when the block interface is placed at the location of the shock wave. Furthermore, the Beam-Warming linearization technique is coupled with a fourth-order compact finite-difference scheme and expanded for 3D problems. The results of the high-order multi-block for the 3D flow field over a NACA 0012 airfoil were also in good agreement with other numerical results.

REFERENCES

Allahyari, M., V. Esfahanian and K.Yousefi (2020). The effects of grid accuracy on flow simulations: A numerical assessment. *Fluids* 5(3), 110.

Allahyari, M. and K. Mohseni (2017). Simulation of compressible flows and shock turbulence interaction using observable Euler and Navier-Stokes equations. *In Proceeding of APS Meeting Abstracts* 62(14), A29.00006.

Allahyari, M. and K. Mohseni (2018). Numerical simulation of flows with shocks and turbulence using observable methodology. In *2018 AIAA Aerospace Sciences Meeting*, Kissimmee, FL, USA, AIAA 2018–0066.

Atta, E. (1981). Component-adaptive grid interfacing. In *19th Aerospace Sciences Meeting*, 382.

Atta, E. H. and J. Vadyak (1982). A grid interfacing zonal algorithm for three-dimensional transonic flows about aircraft configurations. In *Eighth International Conference on Numerical Methods in Fluid Dynamics*, 107–114. Springer.

Beam, R. M. and R. F. Warming (1976). An implicit finite-difference algorithm forhy perbolic systems in conservation-law form. *Journal of Computational Physics* 22(1), 87–110.

Benek, J., J. Steger and F. C. Dougherty (1983). A flexible grid embedding technique with application to the euler equations. In *6th Computational Fluid Dynamics Conference Danvers*, 1944.

Blottner, F. (1975). Investigation of some finite difference techniques for solving the boundary layer equations. *Computer Methods in Applied Mechanics and Engineering* 6(1), 1–30.

Bristeau, M. O., R. Glowinski, J. Periaux, and H. Viviand (1987). *Numerical Simulation of Compressible Navier-Stokes Flows: A GAMM-Workshop*, Volume 18 of *Notes on Numerical Fluid Mechanics*, pp. 183–218. Braunschweig, Germany: Springer.

Colin, O. and M. Rudgyard (2000). Development of high-order taylor–galerkin schemes for les. *Journal of Computational Physics* 162(2), 338–371.

Colonius, T. and S. K. Lele (2004). Computational aeroacoustics: progress on nonlinear problems of sound generation. *Progress in Aerospace sciences* 40(6), 345–416.

Cui, M. (2009). Compact finite difference method for the fractional diffusion equation. *Journal of Computational Physics 228*(20), 7792–7804.

Darwish, M., D. Asmar and F. Moukalled (2004). A comparative assessment within a multigrid environment of segregated pressure-based algorithms for fluid flow at all speeds. *Numerical Heat Transfer, Part B: Fundamentals* 45(1), 49–74.

Deng, X., M. Mao, G. Tu, H. Zhang and Y. Zhang (2012). High-order and high accurate cfd methods and their applications for complex grid problems. *Communications in Computational Physics 11*(4), 1081–1102.

Dennis, S. and J. Hudson (1989). Compact h^4 finite-difference approximations to operators of Navier-Stokes type. *Journal of Computational Physics* 85(2), 390–416.

Douglas, J. and J. E. Gunn (1964). A general formulation of alternating direction methods. *Numerische Mathematik* 6(1), 428–453.

Erlebacher, G., M. Y. Hussaini, C. G. Speziale and T. A. Zang (1992). Toward the large-eddy simulation of compressible turbulent flows. *Journal of Fluid Mechanics* 238, 155–185.

Esfahanian, V., M. Allahyarri and M. Hedayat (2013, December). High order compact finite difference on multiblock domains with parallelization. In 15th *Conference On Fluid Dynamics, fd2013.*, The University of Hormozgan, Bandar Abbas, Iran.

Favini, B., R. Broglia and A. Di Mascio (1996). Multigrid acceleration of second-order eno schemes from low subsonic to high supersonic flows. *International Journal for Numerical Methods in Fluids* 23(6), 589–606.

Freund, J., S. Lele and P. Moin (2000). Numerical simulation of a mach 1.92 turbulent jet and its sound field. *AIAA Journal* 38(11), 2023–2031.

Freund, J. B. (2001). Noise sources in a low reynolds-number turbulent jet at mach 0.9. *Journal of Fluid Mechanics* 438, 277–305.

Gaitonde, D. and M. Visbal (1999). Further development of a Navier-Stokes solution procedure based on higher-order formulas. In *37th Aerospace Sciences Meeting and Exhibit*, pp. 557.

Gaitonde, D. V. and M. R. Visbal (2000). Padetype higher-order boundary filters for the NavierStokes equations. *AIAA Journal* 38(11), 2103– 2112.

Hendriana, D. and K. J. Bathe (2000). On a parabolic quadrilateral finite element for compressible flows. *Computer Methods in Applied Mechanics and Engineering* 186(1), 1–22.

Hessenius, K. A. and M. M. Rai (1986). Applications of a conservative zonal scheme to transient and geometrically complex problems. *Computers & Fluids* 14(1), 43–58.

Hessenius, K. and T. Pulliam (1982). A zonal approach to solution of the euler equations. In *3rd Joint Thermophysics, Fluids, Plasma and Heat Transfer Conference*, pp. 969.

Hirsh, R. S. (1975). Higher order accurate difference solutions of fluid mechanics problems by a compact differencing technique. *Journal of Computational Physics* 19(1), 90–109.

Janenko, N. N. (1971). *The method of fractional steps*. Springer.

Kawai, S. and S. K. Lele (2010). Large-eddy simulation of jet mixing in supersonic crossflows. *AIAA Journal* 48(9), 2063–2083.

Koblitz, A., S. Lovett, N. Nikiforakis and W. D. Henshaw (2017). Direct numerical simulation of particulate flows with an overset grid method. *Journal of Computational Physics* 343, 414–431.

Lele, S. K. (1992). Compact finite difference schemes with spectral-like resolution. *Journal of Computational Physics* 103(1), 16–42.

Li, M., T. Tang and B. Fornberg (1995). A compact fourth-order finite difference scheme for the steady incompressible Navier-Stokes equations. *International Journal for Numerical Methods in Fluids* 20(10), 1137–1151.

Lien, F., W. Chen and M. Leschziner (1996). A multiblock implementation of a non-orthogonal, collocated finite volume algorithm for complex turbulent flows. *International Journal for Numerical Methods in Fluids* 23(6), 567–588.

Morgan, P., M. Visbal and D. Rizzetta (2006). A parallel overset grid high-order flow solver for large eddy simulation. *Journal of Scientific Computing* 29(2), 165–200.

Morgan, P., M. Visbal and K. Tomko (2001). Chimera-based parallelization of an implicit Navier-Stokes solver with applications. In *39th Aerospace Sciences Meeting and Exhibit*, 1088.

Moukalled, F. and M. Darwish (2001). A highresolution pressure-based algorithm for fluid flow at all speeds. *Journal of Computational Physics* 168(1), 101 – 130.

Qiu, J. M. and C. W. Shu (2011). Conservative high order semi-lagrangian finite difference weno methods for advection in incompressible flow. *Journal of Computational Physics* 230(4), 863– 889.

Rahbari, I. and G. Paniagua (2020). Acoustic streaming in turbulent compressible channel flow for heat transfer enhancement. *Journal of Fluid Mechanics* 889, A2.

Rahbari, I. and C. Scalo (2017). Quasi-spectral sparse bi-global stability analysis of compressible channel flow over complex impedance. In *55th AIAA Aerospace Sciences Meeting*, Grapevine, Texas, pp. AIAA 2017–1879.

Rai, M. M. (1986). A conservative treatment of zonal boundaries for euler equation calculations. *Journal of Computational Physics* 62(2), 472–503.

Rai, M. M. and S. R. Chakravarthy (1984). Metricdiscontinuous zonal grid calculations using the osher scheme. *Computers & Fluids* 12(3), 161– 175.

Rizzetta, D. P., M. R. Visbal and P. E. Morgan (2008). A high-order compact finite-difference scheme for large-eddy simulation of active flow control. *Progress in Aerospace Sciences* 44(6), 397–426.

Rousta, F. and B. Lessani (2020). Near-Wall heat transfer of solid particles in particle-laden turbulent flows, *International Communications in Heat and Mass Transfer* (112) 104475.

Schaupp, C., J. Sesterhenn and R. Friedrich (2008). On a method for direct numerical simulation of shear layer/compression wave interaction for aeroacoustic investigations. *Computers & Fluids* 37(4), 463–474.

Sherer, S. and M. Visbal (2007). Multi-resolution implic it large eddy simulations usinga high-order overset-grid approach. *International Journal for Numerical Methods in Fluids* 55(5), 455–482.

Sherer, S. E. and J. N. Scott (2005). High-order compact finite-difference methods on general overset grids. *Journal of Computational Physics* 210(2), 459–496.

Shu, C. W. and S. Osher (1988). Efficient implementation of essentially non-oscillatory shock capturing schemes. *Journal of Computational Physics 77*(2), 439–471.

Shu, C. W. (2016). High order weno and dg methods for time-dependent convection-dominated pdes: A brief survey of several recent developments. *Journal of Computational Physics* 316, 598–613.

Shubin, G., A. Stephens and H. Glaz(1981). Steady shock tracking and Newton's method applied to one-dimensional duct flow. *Journal of Computational Physics* 39(2), 364–374.

Sorenson, R. L. (1982). Grid generation by elliptic partial differential equations for a tri-element augmentor-wing airfoil. *Applied Mathematics and Computation* 10, 653–665.

Spotz, W. and G.Carey (1995). High-order compact scheme for the steady stream-function vorticity equations. *International Journal for Numerical Methods in Engineering* 38(20), 3497–3512.

Steger, J. and R. Sorenson (1979). Automatic mesh point clustering near a boundary in grid generation with elliptic partial differential equations. *Journal of Computational Physics* 33(3), 405 – 410.

Thompson, J. F., F. C. Thames and C. W. Mastin (1974). Automatic numerical generation of body fitted curvilinear coordinate system for field containing any number of arbitrary two-dimensional bodies. *Journal of Computational Physics* 15(3), 299–319.

Visbal, M. R. and D. Rizzetta (2002). Large-eddy simulation on curvilinear grids using compact differencing and filtering schemes. *Journal of Fluids Engineering* 124(4), 836–847.

Visbal, M. R. and D. V. Gaitonde (1999). High order-accurate methods for complex unsteady subsonic flows. *AIAA Journal* 37(10), 1231–1239.

Visbal, M. R. and D. V. Gaitonde (2002). On the use of higher-order finite-difference schemes on curvilinear and deforming meshes. *Journal of Computational Physics* 181(1), 155–185.

Wang, G., F. Duchaine, D. Papadogiannis, I. Duran, S. Moreau and L. Y. Gicquel (2014). An overset grid method for large eddy simulation of turbomachinery stages. *Journal of Computational Physics* 274, 333–355.

Xiong, T., G. Russo and J. M. Qiu (2018). High order multi-dimensional characteristics tracing for the incompressible euler equation and the guiding-center vlasov equation. *Journal of Scientific Computing* 77(1), 263–282.

Yang, H., Z. Chen, A. Przekwas and J. Dudley (2015). A high-order cfd method using successive differentiation. *Journal of Computational Physics* 281, 690–707.

Yang, J., B. Zhang, C. Liang and Y. Rong (2016). A high-order flux reconstruction method with adaptive mesh refinement and artificial diffusivity on unstructured moving/deforming mesh for shock capturing. *Computers & Fluids* 139, 17–35.

Yousefi, K. and A. Razeghi (2018). Determination of the critical Reynolds number for flow over symmetric NACA airfoils. In *2018 AIAA Aerospace Sciences Meeting*, Kissimmee, FL, USA, pp. AIAA 2018–0818.

Zhang, X., G. A. Blaisdell and A. S. Lyrintzis (2004). High-order compact schemes with filters on multi-block domains. *Journal of Scientific Computing* 21(3), 321–339.